Control of vertebrate intraflagellar transport by the planar cell polarity effector Fuz

Eric R. Brooks[1,2] and John B. Wallingford[1,2,3]

[1]Section of Molecular Cell and Developmental Biology, [2]Institute for Cellular and Molecular Biology, and [3]Howard Hughes Medical Institute, University of Texas, Austin, TX 78712

Cilia play key roles in development and homeostasis, and defects in cilia structure or function lead to an array of human diseases. Ciliogenesis is accomplished by the intraflagellar transport (IFT) system, a set of proteins governing bidirectional transport of cargoes within ciliary axonemes. In this paper, we present a novel platform for in vivo analysis of vertebrate IFT dynamics. Using this platform, we show that the planar cell polarity (PCP) effector Fuz was required for normal IFT dynamics in vertebrate cilia, the first evidence directly linking PCP to the core machinery of ciliogenesis. Further, we show that Fuz played a specific role in trafficking of retrograde, but not anterograde, IFT proteins. These data place Fuz in the small group of known IFT effectors outside the core machinery and, additionally, identify Fuz as a novel cytoplasmic effector that differentiates between the retrograde and anterograde IFT complexes.

Introduction

Cilia are microtubule-based cellular protrusions that play key roles in developmental signal transduction, and their dysfunction leads to several human pathologies (Pedersen and Rosenbaum, 2008). Whereas null mutations of core ciliogenesis genes lead to early prenatal lethality, hypomorphic mutations lead to a spectrum of debilitating diseases in humans, known as ciliopathies. Ciliopathic complications include neural tube closure defects, polydactyly, obesity, progressive blindness, and mental retardation (Beales et al., 2007; Arts et al., 2011; Davis et al., 2011).

Ciliogenesis and cilia-mediated signaling both require the function of a highly conserved system of intraflagellar transport (IFT). This system of ∼20 proteins transports ciliary cargoes by engaging specific kinesin and dynein motors to move bidirectionally along the microtubule doublets of the ciliary axoneme (Pedersen and Rosenbaum, 2008; Ishikawa and Marshall, 2011). First identified by pioneering work in the flagellated alga *Chlamydomonas* (Kozminski et al., 1993, 1995), IFT is now known to control cilia biogenesis and function in most ciliated eukaryotes, including vertebrates (Scholey and Anderson, 2006).

Genetic and biochemical studies demonstrate that IFT is subdivided into two complexes: IFT-B, which governs anterograde trafficking from the cell body to the distal tip of the axoneme, and IFT-A, which governs retrograde return (Ishikawa and Marshall, 2011). Loss of a single IFT-B or IFT-A member generally leads to impaired function of the entire subcomplex and a loss of anterograde or retrograde functionality, respectively (Piperno et al., 1998; Pazour et al., 2000; Follit et al., 2006; Qin et al., 2011). Of note, loss of retrograde IFT-A complex function does not seem to prevent anterograde IFT, as cilia are still formed, though they are structurally and functionally compromised (Piperno et al., 1998; Tran et al., 2008; Tsao and Gorovsky, 2008; Qin et al., 2011). This finding suggests not only that that IFT-A and IFT-B functions are separable but also that there may be specific modulators controlling delivery or assembly of anterograde and retrograde IFT complexes.

A small number of factors outside of the core machinery have been found to influence IFT. These include the Bardet–Biedl syndrome proteins BBS-7 and -8, required for motor coordination in *Caenorhabditis elegans* (Blacque et al., 2004; Ou et al., 2005; Pan et al., 2006), Arl13b, a small GTPase required for cohesion of IFT-B and -A subcomplexes (Cevik et al., 2010; Li et al., 2010), Elipsa, which is required for localization of both IFT subcomplexes to basal bodies (Omori et al., 2008), and Ofd1, required to localize IFT88, but not other IFT-B proteins, to basal bodies (Singla et al., 2010).

We and others have shown that the planar cell polarity (PCP) effector Fuz is a critical regulator of cilia structure and

Correspondence to John B. Wallingford: wallingford@mail.utexas.edu

Abbreviations used in this paper: IFT, intraflagellar transport; KD, knockdown; MMR, Marc's modified Ringer's; PCP, planar cell polarity.

The Rockefeller University Press $30.00
J. Cell Biol. Vol. 198 No. 1 37–45
www.jcb.org/cgi/doi/10.1083/jcb.201204072

function in *Xenopus laevis* and mice (Park et al., 2006; Gray et al., 2009; Heydeck et al., 2009; Dai et al., 2011), and, moreover, this locus is implicated in human neural tube closure defects (Seo et al., 2011). The mechanism by which the novel protein encoded by *fuz* governs ciliogenesis remains quite obscure; however, it appears to govern traffic from the cytoplasm to the basal body and then to the ciliary tip (Gray et al., 2009), suggesting that it may interact with the IFT machinery.

Here, we report a novel platform for in vivo time-lapse imaging of IFT in vertebrate multiciliated cells, and we show that loss of Fuz leads to a severe disruption of IFT-B particle dynamics. Interestingly, this phenotype stems from a failure of apical localization of at least one IFT-A complex member and its subsequent failure to enter the axoneme. These data provide the most direct link between a protein associated with PCP and the fundamental machinery of ciliogenesis to date and, additionally, identify Fuz as a novel cytoplasmic effector that differentiates between the retrograde and anterograde IFT complexes.

Results and discussion

We and others have developed *Xenopus* multiciliated cells as a tractable model for in vivo experiments of cilia structure and function. The large size of these cells and their cilia makes them especially amenable to imaging studies (Mitchell et al., 2007; Gray et al., 2009; Kim et al., 2010; Stubbs et al., 2012). Previously, we established that Fuz is essential for ciliogenesis and governs the distal enrichment of the microtubule bundling protein CLAMP (calponin homology and microtubule-associated protein) at the tips of cilia (Fig. 1, a and b; Gray et al., 2009). To further characterize the role of Fuz in cilia, we undertook a quantitative examination of the axonemes of multiciliated cells.

As demonstrated in Fig. 1 a, RFP-CLAMP weakly decorates the entire length of the axoneme but is highly enriched in the distal-most region (Figs. 1 [a and c] and S1 [d and h]). Given that this domain of enrichment was of a consistent length between axonemes and from cell to cell (~2 µm; ~16% of total axoneme length), we refer to this enrichment as the CLAMP compartment.

We then quantified the effect of Fuz knockdown (KD) on this compartment by using a previously validated Fuz antisense morpholino oligonucleotide (Gray et al., 2009). Fuz KD led to a significant reduction in the absolute length of the CLAMP compartment, as compared with controls (~60% reduction; Figs. 1 [c (middle), d (middle), and e] and S1 a). Because Fuz KD also significantly disrupts axoneme length (Figs. 1 e and S1 c), it was possible that this shortening of CLAMP enrichment simply reflected the reduction in axoneme length. However, when we examined the percentage of the axoneme occupied by this compartment, we found that it was significantly reduced in Fuz KD axonemes, as compared with controls (~10% axoneme length in Fuz KD vs. ~16% in controls; Fig. 1 b [right] vs. Fig. 1 a [right] and Fig. 1 d [middle] vs. Fig. 1 c [middle]; also see Figs. 1 e and S1 d) Additionally, in many Fuz KD axonemes, this compartment was completely absent (Figs. 1 b and S1 [a and d]).

Next, we asked whether loss of distal enrichment was specific to CLAMP or whether it represented a more general defect in the distal identity of the axoneme. To address this question, we assayed another microtubule binding protein, EB3, which localizes to the distal tips of cilia and is required for normal cilia structure (Schrøder et al., 2011). We found that GFP-EB3 is enriched to the same distal domain as RFP-CLAMP and, further, that the size of the GFP-EB3 compartment was reduced by >60% upon Fuz KD (Fig. S1 f).

These data could reflect a role for Fuz in the control of distal axoneme identity or, alternatively, a more general role for Fuz in ciliary protein localization. To address this issue, we examined the microtubule-binding domain of MAP7 fused to GFP, which strongly labels a domain in the proximal axoneme of *Xenopus* multiciliated cells (Figs. 1 c [left and right] and S1 h; unpublished data). MAP7-GFP was enriched in a consistent region axoneme to axoneme, and we designate it the MAP7 domain (~2 µm and ~16% axoneme length; Fig. 1 c [right]). In contrast to the CLAMP domain, the absolute size of the MAP7 domain was only slightly perturbed upon Fuz KD (Fig. 1 d [right] vs. Fig. 1 c [right]; also see Figs. 1 e and S1 b). As a result of the shortening of Fuz KD axonemes, however, the relative occupancy of the MAP7 domain was significantly increased (~40% axoneme length in Fuz KD compared with 16% in controls). Thus, disruption of Fuz appears to specifically perturb the distal ends of axonemes in multiciliated cells (Fig. 1 e), and the loss in axoneme length appears to reflect a specific loss of distal axoneme (Fig. 1 e).

The loss of distal identity may reflect a defect in delivery of cargo destined for the CLAMP domain. In this case, a reasonable prediction is that the distal compartments in Fuz KD axonemes would be both shorter and contain a reduced amount of CLAMP. To test this prediction, we exploited the fact that RFP-CLAMP is enriched distally but also weakly labels the entire axoneme, and we measured the intensity of the CLAMP domain normalized against the weaker signal in the axoneme. The CLAMP domain in controls was enriched over fourfold on average over the more proximal axoneme (Fig. 1 f; see Fig. S1 h for methodology). Strikingly, in Fuz KD cilia, this value was reduced by roughly half (Fig. 1 f). Importantly, a similar analysis of MAP7 enrichment showed no change between control and Fuz KD axonemes (Fig. 1 g).

Finally, a trafficking defect within Fuz KD cilia might lead to ectopic CLAMP accumulations in the proximal axoneme. Indeed, examination of CLAMP-RFP intensity profiles along control and Fuz KD axonemes reveals exactly this phenotype, with many KD axonemes exhibiting ectopic enrichments of CLAMP in the more proximal axoneme (Fig. 1 b [right]). Together, these data support a role for Fuz in maintaining ciliary trafficking to the distal axoneme.

Because IFT controls both trafficking within cilia and the integrity of the ciliary distal tip (Marshall and Rosenbaum, 2001; Marshall et al., 2005), we hypothesized that Fuz might modulate IFT dynamics. To test this hypothesis, we developed a system for in vivo imaging of IFT particle movement in the multiciliated cells of the *Xenopus* embryo. We expressed GFP-IFT constructs by targeted injection at low levels, such that no phenotypic effects were observed. Embryos were then mounted and imaged using high-speed confocal microscopy (see Materials

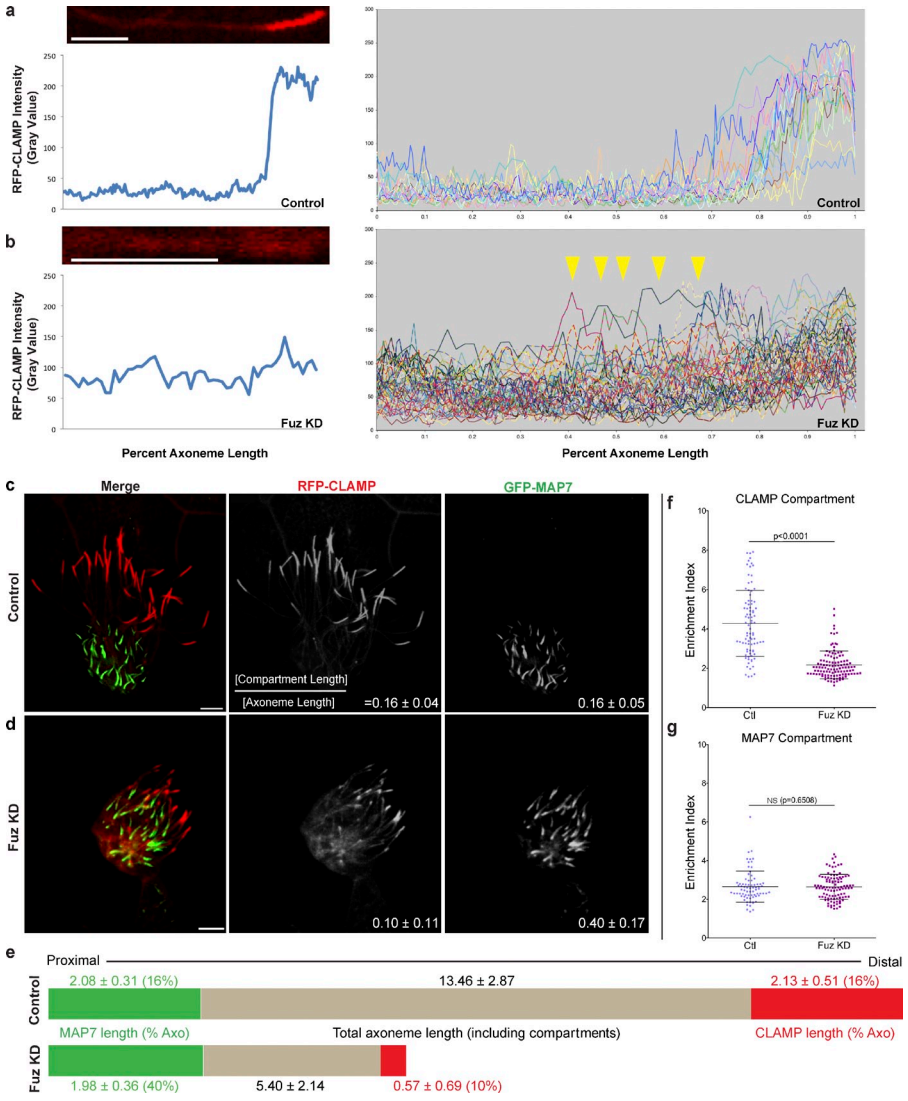

Figure 1. **Fuz is essential for distal, but not proximal, axonemal identity.** (a, left) A representative control axoneme expressing RFP-CLAMP (top) and pixel intensity along the axoneme (bottom). (right) A collection of individual control axonemal intensity plots. (b, left) A representative axoneme from a Fuz KD cell and its corresponding intensity plot. This image is magnified compared with the image in a to facilitate comparison. (right) A collection of intensity plots from individual Fuz KD axonemes. Arrowheads indicate ectopic CLAMP enrichments. (c) Cilia on a control vertebrate multiciliated cell expressing RFP-CLAMP to label the distal axoneme and GFP-MAP7 to label the proximal axoneme. (d) Cilia on a Fuz KD vertebrate multiciliated cell expressing RFP-CLAMP and GFP-MAP7. Also see Fig. S1 (a and b). The mean percentage of axoneme length ± SD occupied by the CLAMP or MAP7 domains is indicated on the bottom right of c (middle [*n* = 54] and right [*n* = 130]) and d (middle [*n* = 52] and right [*n* = 130]). See Fig. S1 (d and e) for quantitation; only axonemes whose whole length was obvious were used for this analysis, and the compartment analysis for this dataset is shown in Fig. S1 g. (a–d) Bars, 3 µm. (e) Schematic representations of control and Fuz KD axonemes (Axo) showing mean proximodistal organization (for quantification, see Fig. S1 [d, e, and g]). Note that in Fuz KD axonemes, the MAP7 domain is of approximately the same length but makes up a greater percentage of the overall shorter axoneme. Also, note the reduction in both length and percentage of occupancy of the CLAMP compartment. Lengths are reported as the mean across the population, and the percentage of occupancies is reported as the mean of ratios from individual axonemes and is therefore not directly comparable. See Materials and methods for details. (f) Fuz KD axonemes show reduced enrichment of RFP-CLAMP signal in the distal domain over basal axoneme levels, as compared with controls (Ctl). Enrichment Index = (mean intensity compartment)/(mean intensity of an equivalent length of nonenriched axoneme). Fuz KD enrichment index (mean ± SD = 2.17 ± 0.70; *n* = 113) versus control enrichment index (4.28 ± 1.68; *n* = 87; P < 0.0001) is shown. Note that only axonemes with discernable distal RFP-CLAMP compartments were used for this analysis. (g) There is no change in the enrichment of the MAP7 compartment between control and Fuz KD axonemes. Fuz KD enrichment index (mean ± SD = 2.64 ± 0.64; *n* = 102) versus control enrichment index (2.65 ± 0.80; *n* = 75; P = 0.6508) is shown.

and methods). Using this method, we were able to consistently track dozens of individual IFT trains within axonemes (Fig. 2 a and Videos 1 and 2).

We first analyzed IFT in controls by imaging GFP fused to IFT20, a member of the IFT-B subcomplex. GFP-IFT20–labeled trains in control axonemes varied in size, consistent with data from *Chlamydomonas* (Engel et al., 2009; Pigino et al., 2009). These trains exhibited a mean anterograde transport rate of 0.84 µm/s and a retrograde transport rate of 0.87 µm/s (Fig. 2, b and c). Compared with *Chlamydomonas*, IFT velocities were rather more variable in *Xenopus* multiciliated cells (Fig. 2, b and c) but were only slightly more variable than those reported for primary cilia in mammalian cells (Besschetnova et al., 2010). Such variation might be explained by the molar differences in the amount of discrete motors attached to IFT particles (Pan et al., 2006).

In addition to anterograde and retrograde movement, IFT in *Chlamydomonas* also involves a remodeling phase at the cilium base (Iomini et al., 2001). Because GFP-IFT20 labels a pool at the basal body in addition to axonemal trains (Follit et al., 2006), we were also able to visualize the release of new anterograde IFT particles from the basal body into the axoneme and the return of retrograde particles from the axoneme into the basal body (Fig. S2 a and Video 3). An additional remodeling phase of the IFT process occurs at the cilium tip, where trains end their anterograde movement and begin retrograde movement (Iomini et al., 2001). We observed in several cases GFP-IFT20–labeled trains that paused and returned retrogradely down the axoneme (Fig. S3 b). In several cases, additional GFP-IFT20–labeled trains could be observed distal to the pausing/reversing trains (Fig. S3 b and Video 4), suggesting that reversal of IFT trains in multiciliated cells does not occur exclusively at the very tip of the ciliary axoneme in these cells, consistent with observations from *Chlamydomonas* (Dentler, 2005). Although these observations are

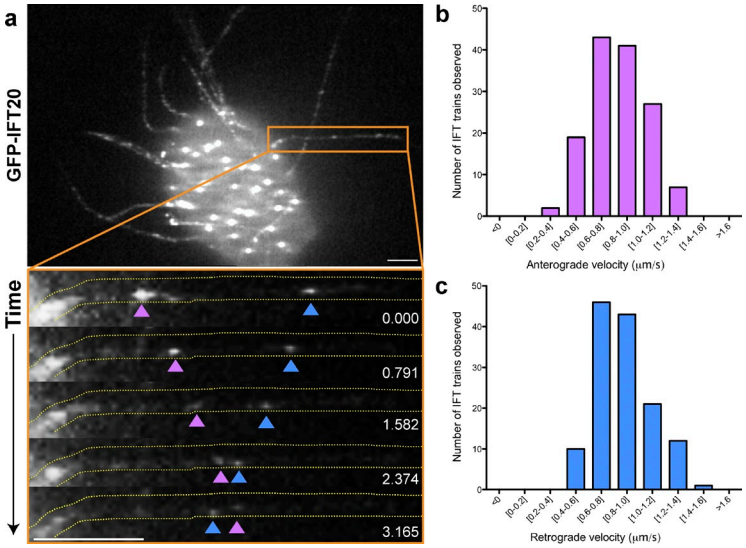

Figure 2. **In vivo imaging of IFT in *Xenopus* multiciliated cells.** (a) Still frame from a video of GFP-IFT20 in a multiciliated cell (Video 1). The orange box indicates the region shown in the bottom image, depicting still frames from a time-lapse video showing processive bidirectional movement of IFT particles in a single control cilium (Video 2). Time is indicated in seconds. Pink arrowheads indicate anterograde particles; blue arrowheads indicate retrograde particles. The axoneme is outlined in yellow. Bars, 3 µm. (b) Histogram of anterograde rates of IFT in *Xenopus* multiciliated cells. (c) Histogram of retrograde rates. (c and d) Mean velocities ± SD are 0.84 ± 0.22 µm/s anterograde (n = 143 trains from 24 cells; six embryos) and 0.87 ± 0.22 µm/s retrograde (n = 125 trains from 25 cells; six embryos). Velocities ranged from 0.36 to 1.35 µm/s anterograde and 0.42 to 1.43 µm/s retrograde. Velocities were calculated as the mean of three independent instantaneous velocities for each reported particle.

not the focus of the current study, they demonstrate the utility of this new platform for analysis of IFT dynamics.

Having established this imaging platform, we found that Fuz KD resulted in profound defects in IFT. In Fuz KD cilia, we observed large accumulations of GFP-IFT20 along the length of the axoneme (Fig. 3, a and c). Time-lapse imaging revealed that these accumulations of GFP-IFT20 were entirely static. Such large, nonmotile IFT trains were never observed in control axonemes, though IFT trains did often pause for short periods (2–4 s). In contrast, the large IFT trains in Fuz KD axonemes remained static during the entire course of our high-speed videos (15–30 s; Fig. 3 a [bottom] and Videos 5 and 6). Moreover, when we made longer videos with conventional confocal microscopy, the accumulations of GFP-IFT20 in Fuz KD axonemes were found to remain static for >4 min, at which point photobleaching precluded further analysis (Fig. 3 d).

Next, we asked whether this defect was specific to IFT20 or whether it was generalizable to another IFT-B, IFT80. IFT trains labeled by GFP-IFT80 behaved identically to GFP-IFT20 trains (Fig. S3 a and Videos 7 and 8). Moreover, we also observed enlarged, nonmotile GFP-IFT80 accumulations upon Fuz KD (Fig. S3 b [top and bottom]).

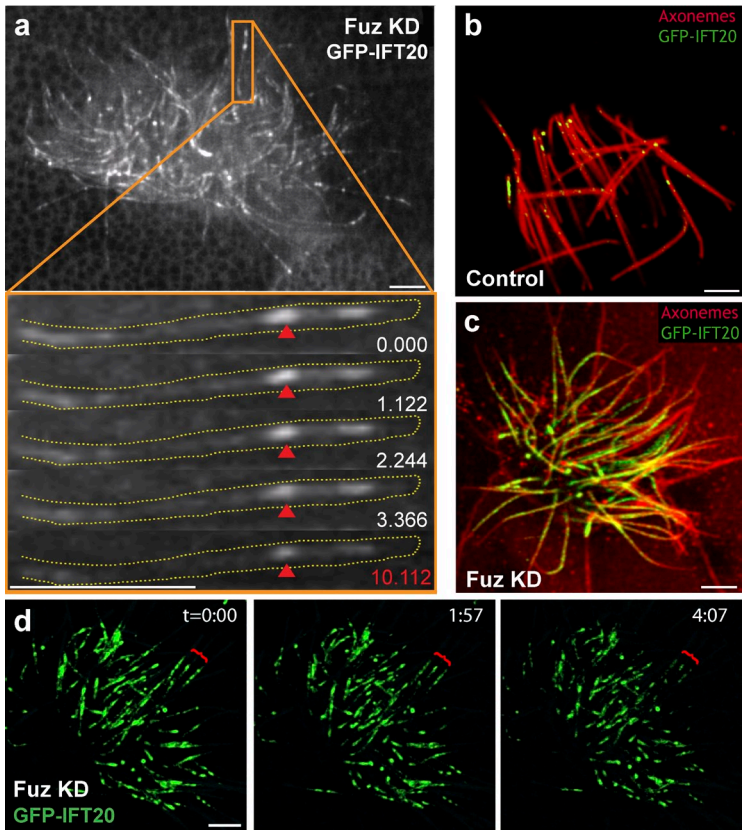

Figure 3. **Loss of Fuz leads to disrupted anterograde IFT.** (a) Still frame from a video of GFP-IFT20 in a Fuz KD cell (Video 5). The orange box indicates the region shown in the bottom image, depicting still frames from a time-lapse video revealing abnormally large and immotile IFT particles (red arrowheads) in a Fuz KD axoneme. The final frame is taken from the end of the time series (Video 6). The axoneme is outlined in yellow. (b) In a fixed control embryo, IFT particles (green) can be seen at low density in the axonemes of a multiciliated cell (red). (c) In a mildly affected Fuz KD embryo, IFT particles accumulate at high density throughout the axonemes. (d) GFP-IFT20 particles are static for >4 min in Fuz KD axonemes. Red brackets indicate especially clear examples. Bars, 4 µm.

Our analysis of IFT-B proteins in Fuz KD axonemes suggests a failure of processive anterograde trafficking. However, loss of anterograde IFT function leads to an absence of cilia (Pazour et al., 2000; Huangfu et al., 2003; Jonassen et al., 2008), whereas Fuz KD results in only shortened cilia. Additionally, the presence of anterograde IFT proteins within the axoneme suggests that IFT-B is partially functional upon loss of Fuz. Photobleached GFP-IFT20 accumulations in Fuz KD axonemes recover some fluorescence over time (unpublished data), suggesting that there is a residual anterograde IFT and indicating that the defects in IFT-B may be indirect.

Therefore, we asked whether Fuz might directly affect the retrograde IFT-A subcomplex by using GFP fused to IFT43, whose human ortholog is mutated in Sensenbrenner syndrome (Arts et al., 2011). This construct localized in a punctate distribution in control cilia, similar to IFT-B members (Fig. 4 a [top and bottom]), and high-speed analysis of GFP-IFT43 in control cilia revealed highly processive bidirectional axonemal traffic (Fig. 4 c [top and bottom] and Videos 9 and 10). In Fuz KD cilia, we observed a severe loss of axonemal GFP-IFT43 localization (Fig. 4 b [top and bottom]) and were unable to detect processive movement of GFP-IFT43 in either direction by high-speed confocal microscopy (Fig. 4 d [top and bottom]).

The specific loss of IFT-A from Fuz KD axonemes was an interesting finding, and we wanted to understand the molecular basis of this phenotype. Given that we previously identified a role for Fuz in trafficking of ciliary proteins from the deeper cytoplasm to the apically localized basal bodies, we hypothesized that Fuz may be necessary for the localization of IFT43 to the apical pools of peri-basal body IFT, where trains are thought to be assembled before they are injected into axonemes (Deane et al., 2001; Ishikawa and Marshall, 2011).

To test this hypothesis, we examined the recruitment of IFT43 to basal bodies by coexpressing GFP-IFT43 and the basal body marker Centrin-RFP and collecting confocal slices just below the apical surface of multiciliated cells. Quantification revealed a dramatic loss of normalized GFP-IFT43 signal from basal bodies in Fuz KD cells, as compared with controls (Fig. 5, a, b, and e; see Fig. S3 c for methodology). We also observed a reduction in the number of GFP-IFT43–labeled foci per multiciliated cell (normalized to the number of Centrin-RFP–labeled basal bodies; Figs. 5 [a and b] and S3 d). Importantly, a similar analysis of GFP-IFT20 recruitment to basal bodies revealed no significant change in either enrichment or number of foci between control and Fuz KD cells (Figs. 5 [c, d, and f] and S3 e).

These findings suggest that the observed defect in IFT-B in Fuz KD axonemes can be attributed to a failure of IFT43, and possibly other retrograde IFT-A complex proteins, to localize appropriately to the peri-basal body pool of IFT proteins. In turn, this failure leads to the failure of IFT-A incorporation into trains loaded into the axoneme (Fig. 4). In this scenario, anterograde IFT will function unidirectionally, facilitating the initial assembly of the axoneme. However, IFT trains will be unable to effect a processive retrograde transition and will become stuck in the axoneme, resulting in the observed accumulations of static IFT-B proteins in the axonemes (Fig. 3). Further, we suggest

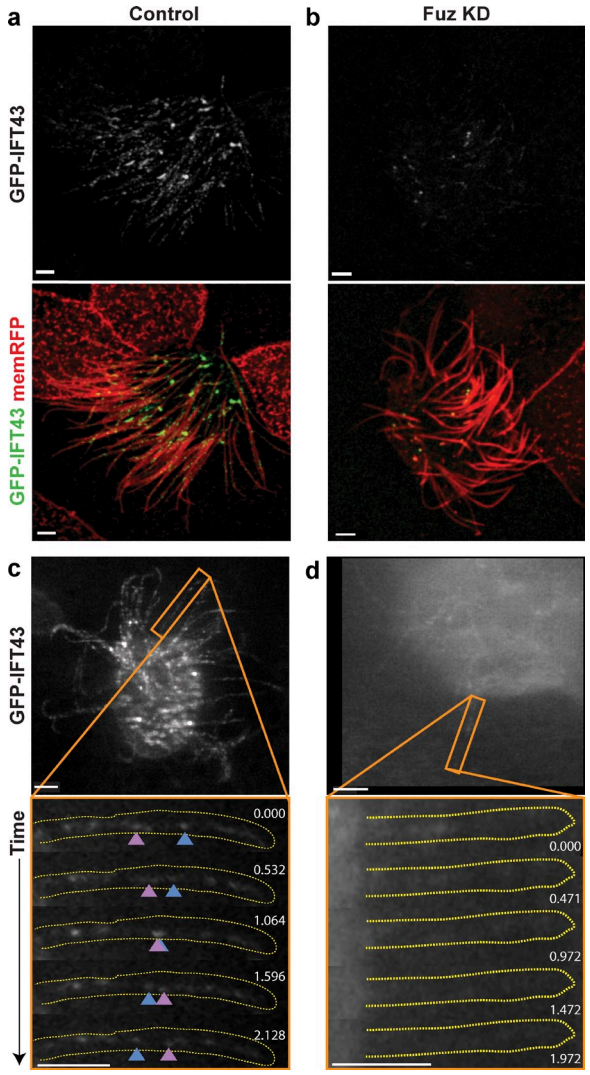

Figure 4. **Fuz is required for the axonemal localization and dynamics of retrograde IFT.** (a) Punctate localization of the IFT-A component GFP-IFT43 in control multiciliated cell axonemes (marked by memRFP). (b) Reduced GFP-IFT43 in the axonemes of Fuz KD multiciliated cells. (c) Still frame from a video of a control multiciliated cell expressing GFP-IFT43 (Video 9). The orange box indicates the region shown in the bottom image, depicting still frames from a video showing processive bidirectional transport in a single control cilium (Video 10). Time is indicated in seconds. Pink arrowheads indicate anterograde particles; blue arrowheads indicate retrograde particles. (d) A single frame from a time-lapse video of a Fuz KD multiciliated cell expressing GFP-IFT43. The image has been intentionally overexposed to bring out the faint background fluorescence of the axonemes. The orange box indicates the region shown in the bottom image, depicting still frames from a video showing loss of GFP-IFT43 dynamics in a single cilium from a Fuz KD multiciliated cell. The axoneme is outlined in yellow. Bars, 3 µm.

that as more IFT-B–dominated trains are injected into the axoneme, they will begin to block transit to the distal tip in a scenario reminiscent of a traffic jam and prevent the delivery of key cargoes (e.g., tubulin dimers, etc.). Because these cargoes are required to maintain cilia length by counterbalancing steady-state disassembly at the tip (Kozminski et al., 1995; Marshall and Rosenbaum, 2001; Ishikawa and Marshall, 2011), impaired delivery can explain both the observed defects in the distal axoneme and the resulting ciliary shortening (Fig. 5 g).

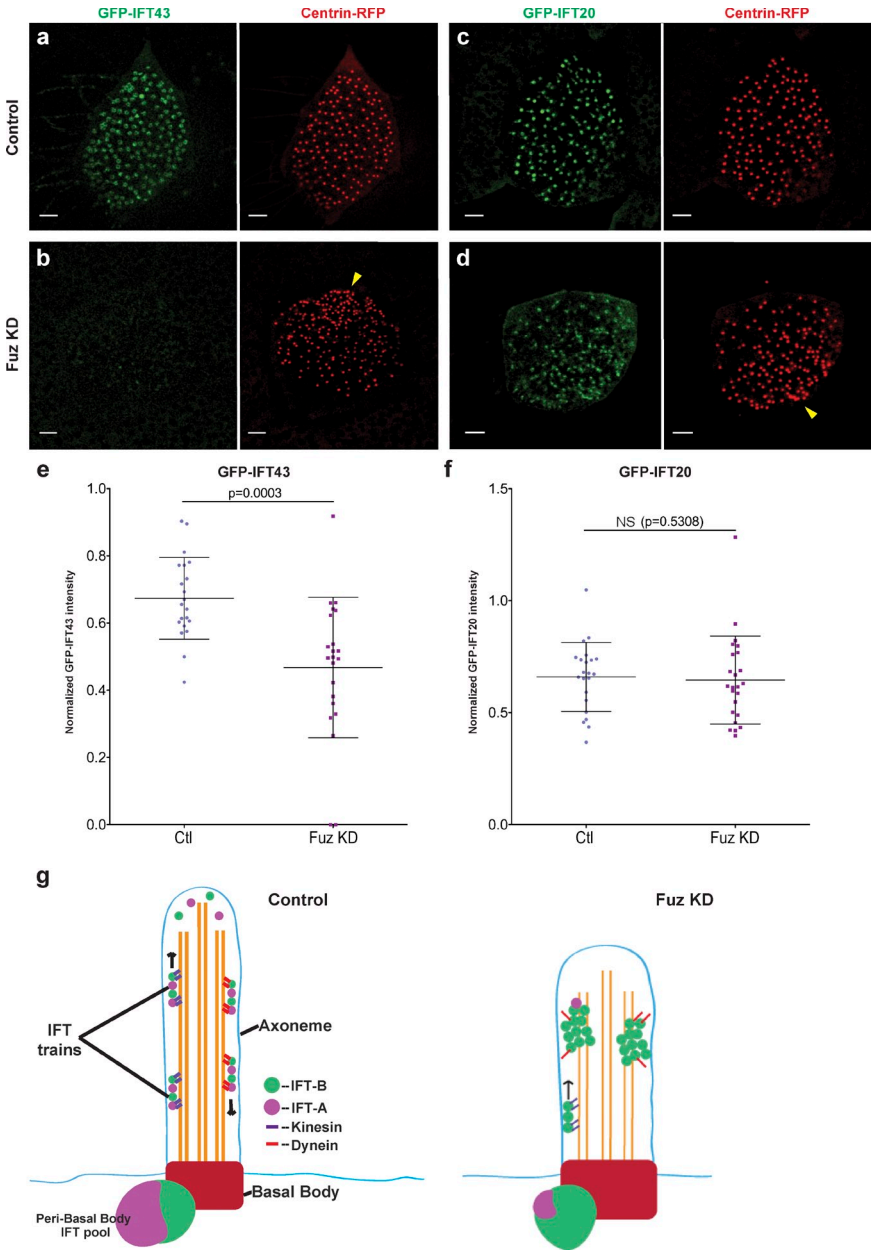

Figure 5. **Fuz is required for the localization of anterograde but not retrograde IFT proteins to peri-basal body pools in the apical cytoplasm.** (a–d) Pools of GFP-IFT43 surrounding basal bodies marked by Centrin-RFP (a, right) in a control cell. Similar pools are observed for GFP-IFT20 (b). GFP-IFT43 pools show reduced enrichment at basal bodies in Fuz KD cells (c). However, GFP-IFT20 is still appropriately localized under the same conditions (d). Note that Fuz KD cells exhibit a second phenotype of basal body clustering (yellow arrowheads in b and d; also see Gray et al. [2009]). Bars, 3 µm. (e) Quantitative comparison of GFP-IFT43 localization in control (Ctl) and Fuz KD cells. Each data point represents the mean of the mean intensities of all GFP-IFT43 pools in a cell normalized to the mean of the mean intensities of all Centrin foci. Fuz KD leads to a significant reduction in GFP-IFT43 localization to apical pools (Fuz KD [mean ± SD = 0.47 ± 0.20; *n* = 21 cells; six embryos] vs. control [mean ± SD = 0.67 ± 0.12; *n* = 21 cells; six embryos; P = 0.0003]). (f) A similar analysis of GFP-IFT20 shows no significant difference in localization between control and Fuz KD cells (Fuz KD [mean ± SD = 0.65 ± 0.20; *n* = 24 cells; six embryos] vs. control [mean = 0.66 ± 0.15; *n* = 22 cells; six embryos; P = 0.5308]). (g) A schematic model of IFT in control and Fuz KD axonemes.

The observed accumulation of IFT-B proteins upon Fuz KD is similar to the phenotype observed upon direct loss of retrograde IFT function (Tran et al., 2008; Tsao and Gorovsky, 2008; Qin et al., 2011). In these contexts, however, IFT-B proteins seem to accumulate preferentially at the distal tip of axonemes, whereas loss of Fuz leads to a more stochastic pattern of IFT accumulations along the entire length of the axoneme (Fig. 3). This stochastic positioning might be explained by partial function of residual IFT-A in Fuz KD axonemes. For example, residual retrograde complexes may allow for only inefficient coherence with dynein, leading trains to disengage and stall randomly along the retrograde trajectory.

These data are the first direct link between a PCP protein and the core, highly conserved machinery of ciliogenesis. In addition, our data place Fuz as one of a small number of known modulators of IFT falling outside of the core biochemical IFT complex. Additionally, the apparent selectivity of Fuz for retrograde IFT places it in an even smaller list of molecules exerting control over a specific subset of IFT proteins. Finally, it is also of interest that Fuz function in this context is evolutionarily restricted; neither *Chlamydomonas* nor *C. elegans* possesses an apparent ortholog of Fuz, and, whereas the *Drosophila melanogaster* genome does contain a Fuz ortholog, it does not appear to function in ciliogenesis. Thus, Fuz may be a vertebrate-specific effector of retrograde IFT function.

These findings substantially expand our understanding of the function of Fuz, a critical regulator of ciliogenesis and developmental signaling (Gray et al., 2009; Heydeck et al., 2009; Dai et al., 2011). Given that a recent study has linked mutation in the locus encoding Fuz with human pathologies (Seo et al., 2011), it will be important to understand how these mutations compromise Fuz function.

More generally, deep analyses of vertebrate IFT dynamics are the critical next step in clarifying poorly understood aspects of this transport, including events at the transition zone, loading and unloading of IFT trains, and low-frequency axonemal behaviors. Such dynamic analysis will be required to understand the molecular etiology of ciliopathic mutations that present without obvious cilia morphology defects (Davis et al., 2011; Rix et al., 2011). The platform we present here allows for the generation of rich datasets at single-train resolutions and will be valuable in elucidating IFT dynamics in both the cell body and the axoneme. Additionally, it is the first platform for IFT analysis in vertebrate multiciliated cells, a population with significant roles in respiration, fertility, and neural morphogenesis, and about which we know comparatively little (Wanner et al., 1996; Banizs et al., 2005; Lyons et al., 2006; Sawamoto et al., 2006).

Here, we have demonstrated that Fuz is required to appropriately localize retrograde IFT proteins within the cytoplasm and thereby maintain cilia. Thus, dynamic spatiotemporal expression of Fuz may be one mechanism by which cells differentiate between ciliated and nonciliated outcomes. Further, this suggests that cytoplasmic control of IFT localization—likely including sequestering of IFT in the deeper cytoplasm as well as regulated assembly of IFT trains—is an important regulatory motif underlying the dynamics of cilia biogenesis, maintenance, and disassembly.

Materials and methods

Embryo manipulations

Female adult *Xenopus* were ovulated by injection of human chorionic gonadotropin, and eggs were fertilized in vitro and dejellied in 3% cysteine (pH 7.9) and subsequently reared in 0.3× Marc's modified Ringer's (MMR; 0.1 M NaCl, 2.0 mM KCl, 1 mM $MgSO_4$, 2 mM $CaCl_2$, and 5 mM Hepes (pH 7.8) in double-distilled H_2O, pH 7.4). For microinjections, embryos were placed in a solution of 2.5% Ficoll (weight/volume) in 0.3% MMR, injected using forceps and an Oxford universal micromanipulator, reared in 2.5% Ficoll in 0.3× MMR to stage 9, and then washed and reared in 0.3× MMR alone (Sive et al., 2000).

Plasmids and cloning

Xenopus IFT20 and IFT80 were identified using Xenbase (Bowes et al., 2008), amplified from cDNA using Phusion High-Fidelity Polymerase (New England Biolabs, Inc.), and subcloned into the CS107-GFP-3Stop backbone by double digestion with XhoI and NotI restriction enzymes. This backbone includes an SP6 promoter and an SV40 polyadenylation signal sequence for in vitro transcription of messenger RNA. *Xenopus* IFT43 provisional sequence was obtained from Xenbase and amplified and subcloned into CS107-3Stop-GFP, as described above. RFP-CLAMP was generated by subcloning of the previously generated CLAMP-GFP (Gray et al., 2009) into CS107-RFP-3Stop backbone. Membrane-RFP (in the CS^{2+} backbone) and Centrin-RFP, GFP-MAP7 (also called GFP-ensconsin; provided by B. Mitchell, Northwestern University, Evanston, IL), and EB3-GFP (each in a CS107-3Stop backbone) were used, as previously reported (Shindo et al., 2008; Gray et al., 2009; Woolner et al., 2009). All constructs were verified by sequencing.

Morpholino and mRNA injections

Capped, polyadenylated mRNA was generated from CS107-3Stop plasmids after linearization by AscI digestion, using the SP6 mMessage mMachine kit (Ambion). The splice-blocking Fuz morpholino (5′-ATCCACTTACTTACCGTAGGACTCC-3′) has been previously described and shown to reduce proper splicing of Fuz, resulting in a truncation of Fuz and loss of Fuz function (Park et al., 2006; Gray et al., 2009). mRNA and/or morpholinos were injected into two ventral blastomeres at the four-cell stage. mRNAs were injected at 50–200 pg per blastomere, and morpholino was injected at 50–60 ng per blastomere.

IFT imaging and quantitation

For high-speed in vivo imaging of IFT, in vitro synthesized capped mRNA was injected into *Xenopus* embryos at the four-cell stage, targeting the ventral/animal blastomeres to ensure expression in the ciliated epidermis. At tailbud stages (approximately stage 25; Nieuwkoop and Faber, 1967), embryos were mounted flank down in 0.8% low–melting point agarose in 0.3× MMR on a round cover glass in specially machined dishes, as described in Kieserman et al. (2010). The motile cilia on multiciliated cells were immobilized by modest pressure exerted by gravity on the embryo against the coverglass. Similar results were obtained when cilia were immobilized on poly-L-lysine–coated coverslips or immobilized by KD of cilia motility factors (Mitchell et al., 2007; unpublished data). Time-lapse series were captured with an inverted confocal microscope (LSM 5 LIVE; Carl Zeiss) using a Plan NeoFluar 100×/1.3 oil immersion objective (Carl Zeiss). All images were acquired at ∼22°C in 1/3× MMR acquired with AIM software (Carl Zeiss), and velocities were measured with Imaris (Bitplane). Velocities were calculated as the mean of three independent instantaneous velocities for each reported particle. For basal body enrichment analysis, embryos expressing Centrin-RFP and the GFP-IFT protein of interest were mounted as described above and imaged using an inverted microscope (LSM 5 PASCAL; Carl Zeiss) with a Fluar 100×/1.3 oil immersion objective (Carl Zeiss). All images were taken at ∼22°C in 1/3× MMR using the AIM software package. Figure images were processed using Imaris and Photoshop (Adobe); all enhancements were applied uniformly to the entire image.

Axoneme compartment imaging

RFP-CLAMP and GFP-MAP7 or GFP-EB3–expressing embryos were mounted as described in the previous section. Images and z series were captured using an inverted confocal microscope (LSM 5 PASCAL) with a Fluar 100×/1.3 oil immersion objective. All images were taken at ∼22°C in 1/3× MMR using AIM software. Figure images were processed using Imaris and Photoshop; all enhancements were applied uniformly to the entire image.

Axoneme compartment analysis and quantification

Axoneme and compartment lengths and intensities were measured from unprocessed images using the Fiji distribution of ImageJ (National Institutes of Health). Raw line intensity plots for CLAMP-RFP were generated by Fiji from hand-drawn lines and normalized and replotted using Excel (Microsoft). Percentage of occupancy was measured at the level of individual axonemes by dividing the length of the enriched CLAMP and/or MAP7 compartments by the total length of that axoneme (measured as the total length of CLAMP-positive signal). Axonemes without an enriched compartment were assigned a compartment length value of 0. As this analysis is performed at the level of single axonemes, the population level mean lengths we report in Fig. 1 e give a slightly less accurate report of actual percentage of occupancy. Enrichment analysis was performed by dividing the mean intensity of the enriched compartment by the mean intensity of an equivalent length of nonenriched axoneme as close to the compartment as possible. All paired datasets were analyzed and plotted with Prism 5 (GraphPad Software). Statistical significance was determined by Mann–Whitney U test analysis.

Basal body IFT enrichment analysis

The 3D object counter plug-in for Fiji was used to detect IFT and Centrin foci in a single-confocal slice just below the apical surface of a single multiciliated cell and to report their mean intensities. Object size was set to 20, and threshold was determined empirically to maximize detection of apparent foci. Data were analyzed and plotted in Prism 5. The mean intensities of all detected GFP-IFT43 or GFP-IFT20 foci in a cell were averaged together and divided by the mean of the mean intensities of all detected Centrin-RFP foci in the same cell to facilitate cross-cell comparisons. Control and Fuz KD paired datasets were tested for statistically significant differences using the Mann–Whitney U test.

Online supplemental material

Fig. S1 shows several quantitative features related to the analysis of cilia length and proximodistal organization in control and Fuz KD cilia. Fig. S2 shows two IFT train behaviors observed in control cilia: the release and return of trains from peri-basal body pools of IFT and midaxonemal pausing. Fig. S3 shows the effect of Fuz KD on the IFT-B protein IFT-80 in *Xenopus* multiciliated cell axonemes. Additionally, this figure demonstrates the methodology used to assess IFT enrichment at basal bodies and shows a quantitative reduction in the number of apical IFT pools in Fuz KD multiciliated cells. Video 1 shows dynamics of GFP-IFT20 in a control multiciliated cell. Video 2 shows a high-magnification view of GFP-IFT20

dynamics in a control axoneme. Video 3 shows dynamics of GFP-IFT20 at the basal body–axoneme junction. Video 4 shows reversal of GFP-IFT20–labeled IFT trains. Video 5 shows large, immotile GFP-IFT20 aggregations in a Fuz KD multiciliated cell. Video 6 shows a high-magnification view of static GFP-IFT20 aggregations in a Fuz KD axoneme. Video 7 shows dynamics of GFP-IFT80 in a control multiciliated cell. Video 8 shows that Fuz KD leads to large, immotile GFP-IFT80 aggregations. Video 9 shows dynamics of GFP-IFT43 in a control multiciliated cell. Video 10 shows a high-magnification view of GFP-IFT20 dynamics in a control axoneme. Online supplemental material is available at http://www.jcb.org/cgi/content/full/jcb.201204072/DC1.

We thank Brian Mitchell for the MAP7-GFP plasmid and for critical reading of this manuscript. We also thank all of our anonymous reviewers for their helpful suggestions, which significantly improved this report.

This work was supported by grants to J.B. Wallingford from the National Institutes of Health/National Institute of General Medical Sciences, The March of Dimes, and The Burroughs Wellcome Fund. J.B. Wallingford is an Early Career Scientist of the Howard Hughes Medical Institute.

Submitted: 13 April 2012
Accepted: 12 June 2012

References

Arts, H.H., E.M.H.F. Bongers, D.A. Mans, S.E.C. van Beersum, M.M. Oud, E. Bolat, L. Spruijt, E.A.M. Cornelissen, J.H.M. Schuurs-Hoeijmakers, N. de Leeuw, et al. 2011. C14ORF179 encoding IFT43 is mutated in Sensenbrenner syndrome. *J. Med. Genet.* 48:390–395. http://dx.doi.org/10.1136/jmg.2011.088864

Banizs, B., M.M. Pike, C.L. Millican, W.B. Ferguson, P. Komlosi, J. Sheetz, P.D. Bell, E.M. Schwiebert, and B.K. Yoder. 2005. Dysfunctional cilia lead to altered ependyma and choroid plexus function, and result in the formation of hydrocephalus. *Development*. 132:5329–5339. http://dx.doi.org/10.1242/dev.02153

Beales, P.L., E. Bland, J.L. Tobin, C. Bacchelli, B. Tuysuz, J. Hill, S. Rix, C.G. Pearson, M. Kai, J. Hartley, et al. 2007. IFT80, which encodes a conserved intraflagellar transport protein, is mutated in Jeune asphyxiating thoracic dystrophy. *Nat. Genet.* 39:727–729. http://dx.doi.org/10.1038/ng2038

Besschetnova, T.Y., E. Kolpakova-Hart, Y. Guan, J. Zhou, B.R. Olsen, and J.V. Shah. 2010. Identification of signaling pathways regulating primary cilium length and flow-mediated adaptation. *Curr. Biol.* 20:182–187. http://dx.doi.org/10.1016/j.cub.2009.11.072

Blacque, O.E., M.J. Reardon, C. Li, J. McCarthy, M.R. Mahjoub, S.J. Ansley, J.L. Badano, A.K. Mah, P.L. Beales, W.S. Davidson, et al. 2004. Loss of *C. elegans* BBS-7 and BBS-8 protein function results in cilia defects and compromised intraflagellar transport. *Genes Dev.* 18:1630–1642. http://dx.doi.org/10.1101/gad.1194004

Bowes, J.B., K.A. Snyder, E. Segerdell, R. Gibb, C. Jarabek, E. Noumen, N. Pollet, and P.D. Vize. 2008. Xenbase: A *Xenopus* biology and genomics resource. *Nucleic Acids Res.* 36:D761–D767. http://dx.doi.org/10.1093/nar/gkm826

Cevik, S., Y. Hori, O.I. Kaplan, K. Kida, T. Toivenon, C. Foley-Fisher, D. Cottell, T. Katada, K. Kontani, and O.E. Blacque. 2010. Joubert syndrome Arl13b functions at ciliary membranes and stabilizes protein transport in *Caenorhabditis elegans*. *J. Cell Biol.* 188:953–969. http://dx.doi.org/10.1083/jcb.200908133

Dai, D., H. Zhu, B. Wlodarczyk, L. Zhang, L. Li, A.G. Li, R.H. Finnell, D.R. Roop, and J. Chen. 2011. Fuz controls the morphogenesis and differentiation of hair follicles through the formation of primary cilia. *J. Invest. Dermatol.* 131:302–310. http://dx.doi.org/10.1038/jid.2010.306

Davis, E.E., Q. Zhang, Q. Liu, B.H. Diplas, L.M. Davey, J. Hartley, C. Stoetzel, K. Szymanska, G. Ramaswami, C.V. Logan, et al. 2011. TTC21B contributes both causal and modifying alleles across the ciliopathy spectrum. *Nat. Genet.* 43:189–196. http://dx.doi.org/10.1038/ng.756

Deane, J.A., D.G. Cole, E.S. Seeley, D.R. Diener, and J.L. Rosenbaum. 2001. Localization of intraflagellar transport protein IFT52 identifies basal body transitional fibers as the docking site for IFT particles. *Curr. Biol.* 11:1586–1590. http://dx.doi.org/10.1016/S0960-9822(01)00484-5

Dentler, W. 2005. Intraflagellar transport (IFT) during assembly and disassembly of *Chlamydomonas* flagella. *J. Cell Biol.* 170:649–659. http://dx.doi.org/10.1083/jcb.200412021

Engel, B.D., W.B. Ludington, and W.F. Marshall. 2009. Intraflagellar transport particle size scales inversely with flagellar length: Revisiting the balance-point length control model. *J. Cell Biol.* 187:81–89. http://dx.doi.org/10.1083/jcb.200812084

Follit, J.A., R.A. Tuft, K.E. Fogarty, and G.J. Pazour. 2006. The intraflagellar transport protein IFT20 is associated with the Golgi complex and is required for cilia assembly. *Mol. Biol. Cell*. 17:3781–3792. http://dx.doi.org/10.1091/mbc.E06-02-0133

Gray, R.S., P.B. Abitua, B.J. Wlodarczyk, H.L. Szabo-Rogers, O. Blanchard, I. Lee, G.S. Weiss, K.J. Liu, E.M. Marcotte, J.B. Wallingford, and R.H. Finnell. 2009. The planar cell polarity effector Fuz is essential for targeted membrane trafficking, ciliogenesis and mouse embryonic development. *Nat. Cell Biol.* 11:1225–1232. http://dx.doi.org/10.1038/ncb1966

Heydeck, W., H. Zeng, and A. Liu. 2009. Planar cell polarity effector gene Fuzzy regulates cilia formation and Hedgehog signal transduction in mouse. *Dev. Dyn.* 238:3035–3042. http://dx.doi.org/10.1002/dvdy.22130

Huangfu, D., A. Liu, A.S. Rakeman, N.S. Murcia, L. Niswander, and K.V. Anderson. 2003. Hedgehog signalling in the mouse requires intraflagellar transport proteins. *Nature*. 426:83–87. http://dx.doi.org/10.1038/nature02061

Iomini, C., V. Babaev-Khaimov, M. Sassaroli, and G. Piperno. 2001. Protein particles in *Chlamydomonas* flagella undergo a transport cycle consisting of four phases. *J. Cell Biol.* 153:13–24. http://dx.doi.org/10.1083/jcb.153.1.13

Ishikawa, H., and W.F. Marshall. 2011. Ciliogenesis: Building the cell's antenna. *Nat. Rev. Mol. Cell Biol.* 12:222–234. http://dx.doi.org/10.1038/nrm3085

Jonassen, J.A., J. San Agustin, J.A. Follit, and G.J. Pazour. 2008. Deletion of IFT20 in the mouse kidney causes misorientation of the mitotic spindle and cystic kidney disease. *J. Cell Biol.* 183:377–384. http://dx.doi.org/10.1083/jcb.200808137

Kieserman, E.K., C. Lee, R.S. Gray, T.J. Park, and J.B. Wallingford. 2010. High-magnification in vivo imaging of *Xenopus* embryos for cell and developmental biology. *Cold Spring Harb Protoc.* 2010:pdb.prot5427. http://dx.doi.org/10.1101/pdb.prot5427

Kim, S.K., A. Shindo, T.J. Park, E.C. Oh, S. Ghosh, R.S. Gray, R.A. Lewis, C.A. Johnson, T. Attie-Bittach, N. Katsanis, and J.B. Wallingford. 2010. Planar cell polarity acts through septins to control collective cell movement and ciliogenesis. *Science*. 329:1337–1340. http://dx.doi.org/10.1126/science.1191184

Kozminski, K.G., K.A. Johnson, P. Forscher, and J.L. Rosenbaum. 1993. A motility in the eukaryotic flagellum unrelated to flagellar beating. *Proc. Natl. Acad. Sci. USA*. 90:5519–5523. http://dx.doi.org/10.1073/pnas.90.12.5519

Kozminski, K.G., P.L. Beech, and J.L. Rosenbaum. 1995. The *Chlamydomonas* kinesin-like protein FLA10 is involved in motility associated with the flagellar membrane. *J. Cell Biol.* 131:1517–1527. http://dx.doi.org/10.1083/jcb.131.6.1517

Li, Y., Q. Wei, Y. Zhang, K. Ling, and J. Hu. 2010. The small GTPases ARL-13 and ARL-3 coordinate intraflagellar transport and ciliogenesis. *J. Cell Biol.* 189:1039–1051. http://dx.doi.org/10.1083/jcb.200912001

Lyons, R.A., E. Saridogan, and O. Djahanbakhch. 2006. The reproductive significance of human Fallopian tube cilia. *Hum. Reprod. Update*. 12:363–372. http://dx.doi.org/10.1093/humupd/dml012

Marshall, W.F., and J.L. Rosenbaum. 2001. Intraflagellar transport balances continuous turnover of outer doublet microtubules: Implications for flagellar length control. *J. Cell Biol.* 155:405–414. http://dx.doi.org/10.1083/jcb.200106141

Marshall, W.F., H. Qin, M. Rodrigo Brenni, and J.L. Rosenbaum. 2005. Flagellar length control system: Testing a simple model based on intraflagellar transport and turnover. *Mol. Biol. Cell*. 16:270–278. http://dx.doi.org/10.1091/mbc.E04-07-0586

Mitchell, B., R. Jacobs, J. Li, S. Chien, and C. Kintner. 2007. A positive feedback mechanism governs the polarity and motion of motile cilia. *Nature*. 447:97–101. http://dx.doi.org/10.1038/nature05771

Nieuwkoop, P.D., and J. Faber. 1994. Normal Table of Xenopus Laevis (Daudin): A Systematical and Chronological Survey of the Development from the Fertilized Egg Till the End of Metamorphosis. Garland Publishing Inc., New York. 252 pp.

Omori, Y., C. Zhao, A. Saras, S. Mukhopadhyay, W. Kim, T. Furukawa, P. Sengupta, A. Veraksa, and J. Malicki. 2008. Elipsa is an early determinant of ciliogenesis that links the IFT particle to membrane-associated small GTPase Rab8. *Nat. Cell Biol.* 10:437–444. http://dx.doi.org/10.1038/ncb1706

Ou, G., O.E. Blacque, J.J. Snow, M.R. Leroux, and J.M. Scholey. 2005. Functional coordination of intraflagellar transport motors. *Nature*. 436:583–587. http://dx.doi.org/10.1038/nature03818

Pan, X., G. Ou, G. Civelekoglu-Scholey, O.E. Blacque, N.F. Endres, L. Tao, A. Mogilner, M.R. Leroux, R.D. Vale, and J.M. Scholey. 2006. Mechanism of transport of IFT particles in *C. elegans* cilia by the concerted action of kinesin-II and OSM-3 motors. *J. Cell Biol.* 174:1035–1045. http://dx.doi.org/10.1083/jcb.200606003

Park, T.J., S.L. Haigo, and J.B. Wallingford. 2006. Ciliogenesis defects in embryos lacking inturned or fuzzy function are associated with failure of planar cell polarity and Hedgehog signaling. *Nat. Genet.* 38:303–311. http://dx.doi.org/10.1038/ng1753

Pazour, G.J., B.L. Dickert, Y. Vucica, E.S. Seeley, J.L. Rosenbaum, G.B. Witman, and D.G. Cole. 2000. *Chlamydomonas IFT88* and its mouse homologue, polycystic kidney disease gene *Tg737*, are required for assembly of cilia and flagella. *J. Cell Biol.* 151:709–718. http://dx.doi.org/10.1083/jcb.151.3.709

Pedersen, L.B., and J.L. Rosenbaum. 2008. Intraflagellar transport (IFT) role in ciliary assembly, resorption and signalling. *Curr. Top. Dev. Biol.* 85:23–61. http://dx.doi.org/10.1016/S0070-2153(08)00802-8

Pigino, G., S. Geimer, S. Lanzavecchia, E. Paccagnini, F. Cantele, D.R. Diener, J.L. Rosenbaum, and P. Lupetti. 2009. Electron-tomographic analysis of intraflagellar transport particle trains in situ. *J. Cell Biol.* 187:135–148. http://dx.doi.org/10.1083/jcb.200905103

Piperno, G., E. Siuda, S. Henderson, M. Segil, H. Vaananen, and M. Sassaroli. 1998. Distinct mutants of retrograde intraflagellar transport (IFT) share similar morphological and molecular defects. *J. Cell Biol.* 143:1591–1601. http://dx.doi.org/10.1083/jcb.143.6.1591

Qin, J., Y. Lin, R.X. Norman, H.W. Ko, and J.T. Eggenschwiler. 2011. Intraflagellar transport protein 122 antagonizes Sonic Hedgehog signaling and controls ciliary localization of pathway components. *Proc. Natl. Acad. Sci. USA*. 108:1456–1461. http://dx.doi.org/10.1073/pnas.1011410108

Rix, S., A. Calmont, P.J. Scambler, and P.L. Beales. 2011. An Ift80 mouse model of short rib polydactyly syndromes shows defects in hedgehog signalling without loss or malformation of cilia. *Hum. Mol. Genet.* 20:1306–1314. http://dx.doi.org/10.1093/hmg/ddr013

Sawamoto, K., H. Wichterle, O. Gonzalez-Perez, J.A. Cholfin, M. Yamada, N. Spassky, N.S. Murcia, J.M. Garcia-Verdugo, O. Marin, J.L.R. Rubenstein, et al. 2006. New neurons follow the flow of cerebrospinal fluid in the adult brain. *Science*. 311:629–632. http://dx.doi.org/10.1126/science.1119133

Scholey, J.M., and K.V. Anderson. 2006. Intraflagellar transport and cilium-based signaling. *Cell.* 125:439–442. http://dx.doi.org/10.1016/j.cell.2006.04.013

Schrøder, J.M., J. Larsen, Y. Komarova, A. Akhmanova, R.I. Thorsteinsson, I. Grigoriev, R. Manguso, S.T. Christensen, S.F. Pedersen, S. Geimer, and L.B. Pedersen. 2011. EB1 and EB3 promote cilia biogenesis by several centrosome-related mechanisms. *J. Cell Sci.* 124:2539–2551. http://dx.doi.org/10.1242/jcs.085852

Seo, J.H., Y. Zilber, S. Babayeva, J. Liu, P. Kyriakopoulos, P. De Marco, E. Merello, V. Capra, P. Gros, and E. Torban. 2011. Mutations in the planar cell polarity gene, Fuzzy, are associated with neural tube defects in humans. *Hum. Mol. Genet.* 20:4324–4333. http://dx.doi.org/10.1093/hmg/ddr359

Shindo, A., T.S. Yamamoto, and N. Ueno. 2008. Coordination of cell polarity during *Xenopus* gastrulation. *PLoS ONE*. 3:e1600. http://dx.doi.org/10.1371/journal.pone.0001600

Singla, V., M. Romaguera-Ros, J.M. Garcia-Verdugo, and J.F. Reiter. 2010. Ofd1, a human disease gene, regulates the length and distal structure of centrioles. *Dev. Cell*. 18:410–424. http://dx.doi.org/10.1016/j.devcel.2009.12.022

Sive, H.L., R.M. Grainger, and R.M. Harland. 2000. Early development of Xenopus laevis: a laboratory manual. Cold Spring Harbor Laboratory Press, Cold Spring Harbor, NY. 338 pp.

Stubbs, J.L., E.K. Vladar, J.D. Axelrod, and C. Kintner. 2012. Multicilin promotes centriole assembly and ciliogenesis during multiciliate cell differentiation. *Nat. Cell Biol.* 14:140–147. http://dx.doi.org/10.1038/ncb2406

Tran, P.V., C.J. Haycraft, T.Y. Besschetnova, A. Turbe-Doan, R.W. Stottmann, B.J. Herron, A.L. Chesebro, H. Qiu, P.J. Scherz, J.V. Shah, et al. 2008. THM1 negatively modulates mouse sonic hedgehog signal transduction and affects retrograde intraflagellar transport in cilia. *Nat. Genet.* 40:403–410. http://dx.doi.org/10.1038/ng.105

Tsao, C.-C., and M.A. Gorovsky. 2008. Tetrahymena IFT122A is not essential for cilia assembly but plays a role in returning IFT proteins from the ciliary tip to the cell body. *J. Cell Sci.* 121:428–436. http://dx.doi.org/10.1242/jcs.015826

Wanner, A., M. Salathé, and T.G. O'Riordan. 1996. Mucociliary clearance in the airways. *Am. J. Respir. Crit. Care Med.* 154:1868–1902.

Woolner, S., A.L. Miller, and W.M. Bement. 2009. Imaging the cytoskeleton in live *Xenopus laevis* embryos. *Methods Mol. Biol.* 586:23–39. http://dx.doi.org/10.1007/978-1-60761-376-3_2